MICROSCOPY

Microscopy, 2015, 37–44
doi: 10.1093/jmicro/dfu102
Advance Access Publication Date: 17 December 2014

Review

Connectome of the fly visual circuitry

Shin-ya Takemura*

Janelia Research Campus, Howard Hughes Medical Institute, 19700 Helix Drive, Ashburn, VA 20147, USA

*To whom correspondence should be addressed. E-mail: takemuras@janelia.hhmi.org

Received 7 October 2014; Accepted 13 November 2014

Abstract

Recent powerful tools for reconstructing connectomes using electron microscopy (EM) have made outstanding contributions to the field of neuroscience. As a prime example, the detection of visual motion is a classic problem of neural computation, yet our understanding of the exact mechanism has been frustrated by our incomplete knowledge of the relevant neurons and synapses. Recent connectomic studies have successfully identified the concrete neuronal circuit in the fly's visual system that computes the motion signals. This identification was greatly aided by the comprehensiveness of the EM reconstruction. Compared with light microscopy, which gives estimated connections from arbor overlap, EM gives unequivocal connections with precise synaptic counts. This paper reviews the recent study of connectomics in a brain of the fruit fly *Drosophila* and highlights how connectomes can provide a foundation for understanding the mechanism of neuronal functions by identifying the underlying neural circuits.

Key words: EM reconstruction, synaptic circuits, neural computation, motion detection, insect vision, medulla

Introduction

In neuroscience research, discoveries over the past few decades in the fruit fly *Drosophila* have made great contributions to our understanding of the mechanisms behind nervous system function [1–3]. Recently, a unique combination of genetic, anatomical and physiological tools available in *Drosophila* [4] has accelerated research regarding functions of neural circuits. For instance, mechanisms of detecting visual motion are currently subject to intense behavioral, physiological and anatomical investigations in this species (reviewed in [5, 6]).

It has been nearly 60 years since an influential model of visual motion detection, the Hassenstein–Reichardt elementary motion detector (EMD) (Fig. 1a), was proposed by two German scientists [7, 8]. This computational model was originally proposed based upon experiments of the optomotor behavior in insects, and thereafter had also been applied to explain motion detection in different species, including man (for review, see [9]). The idea was that the nervous system contains many of these local computational units, which collectively cover the entire visual field, each extracting locally the direction of image motion. The circuits shown in Fig. 1a respond to rightward motion because light input into the left channel of two adjacent facets is transmitted with an additional delay relative to that into the right channel. Thus the signals from both channels will be closely aligned in time when they arrive at the downstream multiplication unit so that the signals become amplified nonlinearly. As a result, the model responds preferentially to the rightward motion, and a similar computation detects leftward motion.

Since the initial EMD model was released, the local motion detection has been a focus of successive theoretical [10–13] and experimental [14–24] studies for more than

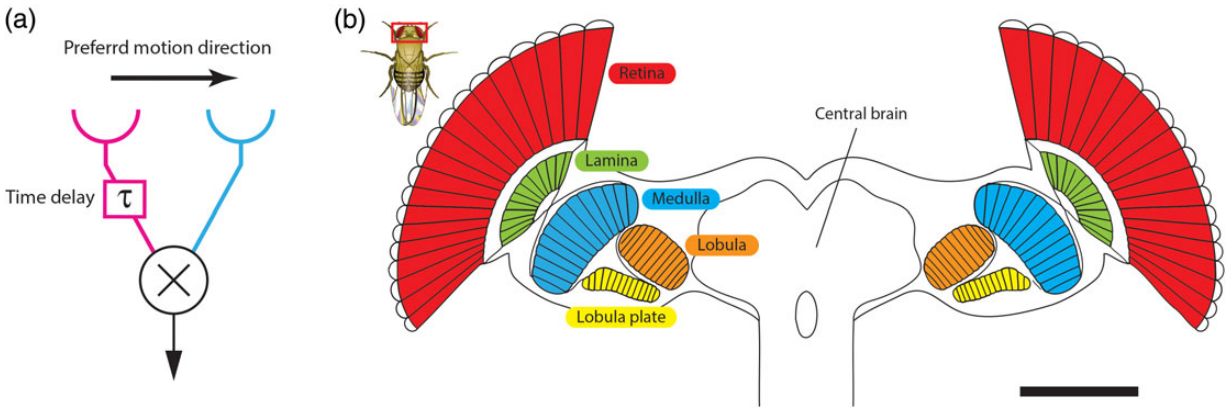

Fig. 1. Visual motion detection in the *Drosophila* visual system. (a) Rightward motion component of Hassenstein–Reichardt EMD model. Light input into the left channel (magenta) is transmitted with an additional delay, relative to the input to the right channel (cyan). The signals from both channels therefore will arrive at the downstream multiplication unit closer in time to each other, and accordingly the signals become enhanced nonlinearly. (b) Diagram of horizontal section of the fly's brain and visual system. Fly's optic lobe consists of four retinotopically organized neuropils: the lamina, medulla, lobula and lobula plate. Scale bar = 100 μm.

half a century. These conclusions were largely consistent with the original proposal of the EMD model. However, until recently, the EMD circuit had never been fully mapped onto the concrete neural elements. Thus, for many decades, we have not had conclusive evidence that those computations indeed occur in the actual nervous system.

A visual system in *Drosophila*

In the insect visual system, the image of the environment formed by retina's optics is then transmitted to the visual centers or optic lobe. Both the retina and optic lobe have specialized morphologies and functions to perform their tasks. In the fly, the optic lobe is composed of four retinotopically organized neuropils; the lamina, medulla, lobula and lobula plate (Fig. 1b). Where is the EMD circuit present in the optic neuropils? EMD circuits should lie at least partly within the medulla, the second optic neuropil, as shown by the following two lines of experimental evidence.

First, neither photoreceptors nor cells in the upstream lamina show any directional selectivity [25–28]. Second, the immediate downstream neuropil, the lobula plate, contains large 'lobula plate tangential cells' which exhibit strong directional selectivity [29]. These lobula plate cells integrate local motion signals to produce wide-field motion response [29, 30]. These results suggest that the motion signals are computed somewhere in between the lamina and the lobula plate. Therefore it is essential to identify the neural circuits in the medulla, but the medulla neuropil has been an impenetrable region for a long time because of its size, neural complexity and difficulty of neurophysiological approaches.

In the fly, each optic neuropil is an array of repeating modules corresponding to the hexagonal lattice of ommatidia in the compound eye [31–34]. In the medulla, each unit module, called a medulla column, receives stereotypic columnar projections of lamina neurons [32]. These input projections contain a pair of lamina cell types, L1 and L2, together required for a fly to sense motion [23, 35, 36], after receiving direct input from photoreceptors in the lamina [37]. However, L1 and L2 themselves do not possess any directional selectivity [38, 39]. Thus, we should examine the downstream medulla neurons to identify the circuits computing motion signals. The medulla houses more than 60 different cell types, reported in the previous Golgi impregnation study [40].

Connectome reconstruction using serial-section transmission electron microscopy

To identify the target medulla neurons postsynaptic to L1 and L2 and provide the reliable foundation for further comprehensive analysis on visual motion processing, a complete, dense connectome of a single medulla column was reconstructed using serial-section electron microscopy (serial-EM) [41]. To date, serial-EM reconstruction remains the only reliable method to determine neural circuits at the level of synapses [42]. There are three established imaging techniques for serial-EM reconstruction: (i) serial block-face electron microscopy (SBEM) [43], (ii) focused ion beam scanning electron microscopy (FIB-SEM) [44] and (iii) serial-section transmission electron microscopy (ssTEM) (e.g. [31, 42]). The method of ssTEM was employed for the medulla reconstruction since it provides the best $x-y$ resolution of images; that seemed advantageous for identification of tens of thousands of synapses.

However, one obstacle to serial-EM reconstruction is the need for processing massive amounts of EM data. To

reconstruct the volume of interest in an appropriate time scale, a high-throughput, semi-automated reconstruction pipeline was deployed for ssTEM [45], then applied to the medulla reconstruction.

Semi-automated reconstruction pipeline

Connectome reconstruction using ssTEM is a multi-stage process, starting with tissue preparation. The medulla tissue was fixed by high-pressure freezing followed by freeze-substitution, which preserved the native structure of specimens to a greater extent than conventional methods [46]. The well-preserved tissue provides greater accuracy at each stage of the reconstruction pipeline. Then, more than 2000 serial sections were cut through the entire depth of the medulla, each roughly 40 nm thick (total sectioning time, 144 h). Three sections were lost during collection. Within each section, a 90 × 90 μm field was imaged at the resolution of 3.1 × 3.1 nm per pixel, taking 65 days. The image resolution was sufficient to identify chemical synapses for both pre- and postsynaptic sites.

The acquired EM image stack was then processed in the reconstruction pipeline that consisted of five main tasks: alignment, 2D segmentation, 3D linkage, synapse annotation and proofreading.

Alignment

The separately acquired EM images of different sections and different parts from the same section need to be registered. First, all overlapping image pairs, both in a single section and between consecutive sections, are aligned pairwise. Next, the transformed images are fit into a global coordinate system via a least-squares fit, then slightly warped to avoid discontinuities at image seams (see [47] for details). An accurate image alignment is critical for the rest of the automated processes as well as the later manual proofreading. Although most image defects can be handled automatically, some images have artifacts, such as section folds, that need extra care. In retrospect, because of these artifacts and image distortions, ssTEM has little or no advantage over the other SBEM or FIB-SEM techniques, despite its higher resolution.

2D segmentation

Segmentation is the task that partitions an image into 'meaningful' sets of pixels, which in this case are distinct neural processes. In a TEM dataset, given that the resolution of the image stack is anisotropic (40 nm in z, 3.1 nm in x–y), 2D image segmentation is executed first, followed by cross-section linkage in 3D. The boundaries of each neuronal profile were segmented by automated algorithms developed using different segmentation techniques [48–52]. This auto-segmentation produces two kinds of errors: (i) false boundaries or over-segmentations, and (ii) missing boundaries or under-segmentations. Decreasing either of these errors leads to an increase of the other, resulting in a trade-off. Given that the errors of over-segmentation are easier to fix in the manual proofreading than those of under-segmentation, the automatic algorithms were tuned to produce an over-segmented image volume. Such settings are also beneficial since they segment small and thin processes more precisely. Those processes are particularly crucial to the accurate connectivity map because there are many small profiles at synaptic sites.

3D linkage

3D linkage identifies pairs of segments in adjacent sections that are likely to belong to the same neuron, and links all the pairs to assemble 3D shapes of neurons. Our automated 3D linkage constructed a linkage graph of consecutive segments based on evaluating their proximity and similarity [53]. The accuracy of linkage is highly dependent on the quality of section alignment and 2D segmentation.

Synapse annotation

To map all the chemical synapses in the volume, presynaptic active zones must be identified. In the *Drosophila* visual system, these are composed of presynaptic T-bar ribbon, often seen as T-shaped structure. In invertebrates such as *Drosophila* and *Caenorhabditis elegans*, it is common for one presynaptic site to signal several postsynaptic sites. In the medulla, each T-bar is typically associated with three to eight postsynaptic partners. These postsynaptic terminals are recognized by their postsynaptic densities (PSDs), and then assigned to their corresponding T-bar. A total of more than 10 000 T-bars and 38 000 postsynaptic sites were annotated in the reconstructed volume, taking ∼300 person-hours. Although the existence of gap-junctional coupling between particular cell types was proposed previously [36], no such structure was found in this EM preparation. The ultrastructure of candidate gap junctions is perhaps fewer clear than chemical synapses. More examination should validate the presence of gap junctions in the future study.

Proofreading

Finally, the errors resulting from the above automatic segmentation and linkage processes are corrected manually. There are two major tasks in this step: (i) fixing errors of 2D segmentation and 3D linkage to generate precise neuron shape reconstructions, and (ii) tracing postsynaptic terminals sparsely. As described above, postsynaptic processes at synaptic sites are often extremely small, and hence it is not an easy task to segment and link them fully automatically.

To provide meaningful synaptic connectivity, each postsynaptic terminal must be checked to be sure it is assigned to its parent neuron correctly.

Although effort continues to improve the accuracy of each automation step, the proofreading tasks are still fairly time-consuming. It is therefore essential to have technical support from a group of professional editors, referred to as proofreaders, whose work is supervised by expert biologists. To increase the reliability of the sparse tracing, two proofreaders are assigned to each synapse. Then two connectomes from the dual proofreader results were generated: an inclusive version that included connections found by either proofreader, and a consensus version in which connections were accepted only when both proofreaders agreed. Although the inclusive connectome had ~16% more connections, all the additional connections had only one synaptic contact. All connections with two or more synapses were present in both connectomes. The analysis of medulla circuits used the consensus connectome, but the conclusions remained unchanged when using the inclusive connectome.

Cell identification from the reconstruction

Given the time-consuming nature of EM reconstructions, the smallest possible medulla volume is required. Thus, an initial reconstruction target was chosen as $10 \times 10 \times 50\ \mu m^3$ volume that permits a reconstruction of periodic module of the medulla, a single medulla column. Within this volume, the target column is densely reconstructed. The reconstruction volume is then expanded in order to trace some specific connections between columns. Accordingly, the final reconstruction volume becomes $37 \times 37 \times 50\ \mu m^3$, in which the surrounding 18 columns were sparsely reconstructed.

A total of 379 neurons were reconstructed in the medulla volume (Fig. 2a). To map the reconstruction onto the existing body of knowledge, the reconstructed bodies are assigned to specific cell types previously proposed by light microscopy. By matching the shapes of arbors with those in the previous studies using Golgi impregnation [39] or more recent confocal microscopy of genetically labeled single cells (GSC) [41], 56 distinct cell types are identified unequivocally among the reconstructed neurons (Fig. 2b). Each of them is morphologically unique. This includes the cell types for which a Golgi counterpart could not be found but which are validated using isomorphs from GSC labeling. Each of these cells is newly named and added to a medulla cell type library.

Candidate motion detection circuit in the medulla

By combining the neural body identifications with synapse annotation, a medulla connectome module was generated

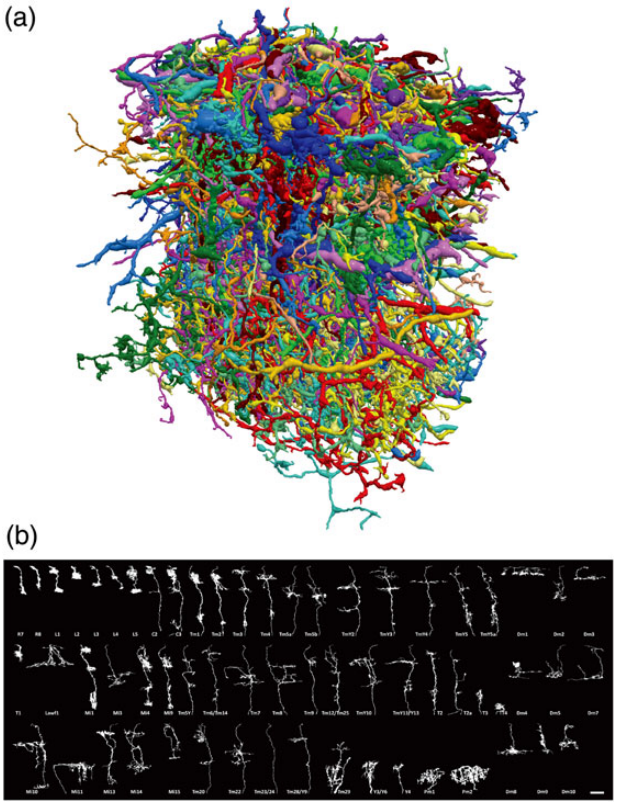

Fig. 2. Neuron reconstructions in the medulla. (a) A total of 379 neurons reconstructed in the medulla volume. The dense reconstruction in the initial volume, with the additional sparse reconstruction in the expanded volume, was acquired for comprehensive analysis of medulla circuits. (b) Cell types identified from the medulla reconstruction. The shapes of arbors of reconstructed neurons are compared with those reported from light microscopy. In many cases, a reconstructed cell is nicely matched to the previously proposed cell type from Golgi impregnation study [39]. Some other reconstructions do not have any Golgi counterpart but they are validated using isomorphs from more recent confocal microscopy using a genetic approach (see [41] for details). Scale bar = 10 μm.

(Fig. 3a). The connectome showed two medulla cell types, Mi1 and Tm3, as postsynaptic targets of L1. It also revealed the downstream connections of Mi1 and Tm3 to columnar T4 neurons (Fig. 3a and b).

Several lines of evidence indicate that the motion signals are relayed to the lobula plate via T4 cells [38, 55–58]. A T4 cell has a unique morphology, having the dendrites in the deepest layer of the medulla (stratum M10), and extending two axonal projections into the lobula plate where one makes terminal arbors within the neuropil, with another process extending further to the end at its cell body location outside the neuropil. A study using optical recordings on T4 cells demonstrated that specific subpopulations of T4s are directionally tuned to one of the four cardinal directions: upward, downward, forward and backward [59]. Those direction preferences of T4s are also differentiated by their terminal arbors in the lobula plate's four sublayers, i.e. Lp1, Lp2, Lp3 and Lp4 are responsible for motion front-to-back,

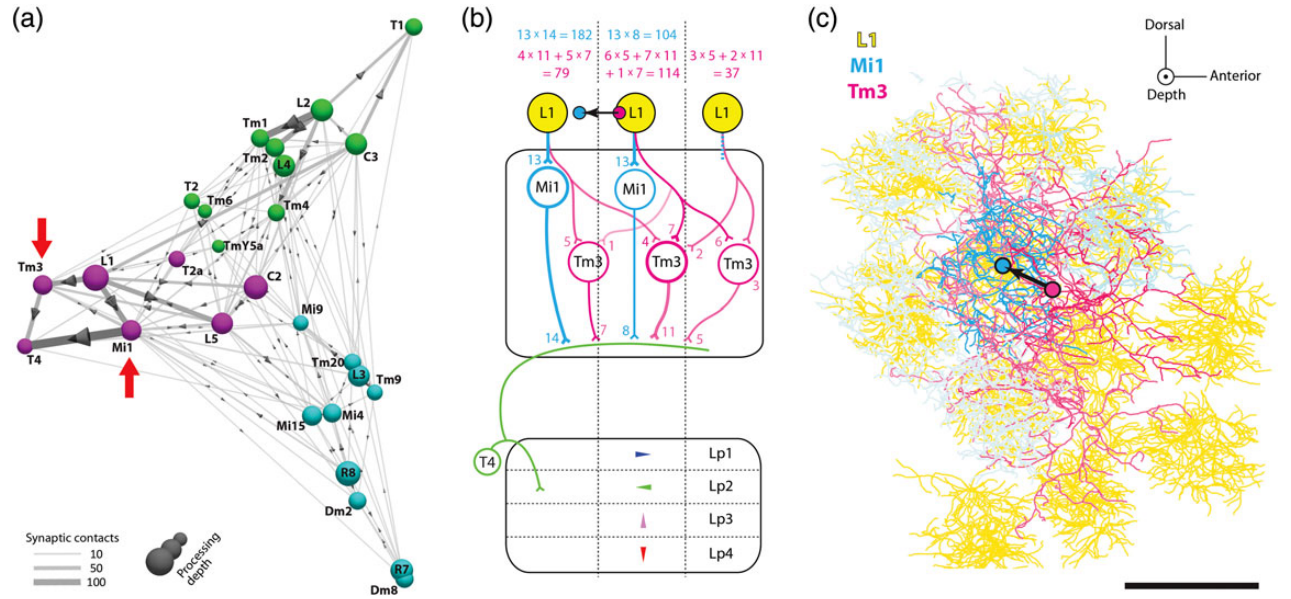

Fig. 3. Motion detection circuit revealed by the medulla connectome. (a) 3D graph representation of medulla connectome module. Cell types with stronger connections are positioned closer to each other, using the visualization of similarities layout algorithm [54]. Clear separation is observed between the pathways of L1 (spheres in purple) and L2 (spheres in green). The medulla connectome reconstruction identified two medulla cell types, Mi1 and Tm3 (red arrows), as the two strongest paths bridging between L1 and L4. (b) Schematic representation of inputs to a single T4 cell through Mi1 and Tm3 cells. Mock synaptic weights illustrate how the receptive fields are calculated (see the main text for details). The connectome-based T4 receptive field strongly suggests that inputs to T4 from Mi1 and Tm3 cells implement the two arms of a motion detector. (c) Cross-section view of dendritic arbors of Mi1 (cyan) and Tm3 (magenta), overlaid on the array of L1 terminals (yellow). The color saturation reflects the number of synaptic contacts made onto the T4. T4 receptive fields of Mi1 component and Tm3 component overlap substantially with one another, but these receptive fields are significantly displaced when they are calculated as illustrated in b. The direction of displacements (arrow, the vector is fly's backward in this case) correlates with the direction preference of the T4 on the assumption that the displacement vector is from the Tm3 center of mass to the Mi1 center of mass. Scale bar in *c* = 8 μm. Figure panels are modified after Takemura *et al.* [41].

back-to-front, down-to-up and up-to-down, respectively (Fig. 3b).

Since the medulla connectome accurately captures not only the presence but also the absence of strong connections between any two cell types, Mi1 and Tm3 inputs to T4 are known to be the two strongest paths bridging between L1 and T4. It is thus hypothesized that Mi1 and Tm3 inputs to T4 implement the two arms of a motion detector (Fig. 3b, details are as given below).

Anatomical receptive fields of T4 cells

To explore whether Mi1 and Tm3 converging onto T4 cells could constitute the two arms of a motion detector, connections from individual Mi1 and Tm3 neurons onto the T4 cell in question were analyzed. It revealed that each T4 receives input from multiple Mi1s and Tm3s in the medulla, suggesting that, unlike the circuit in the EMD model, several points in the visual field constitute each arm of the motion detector (Fig. 3b). To determine the visual receptive fields of T4 inputs more in detail, synaptic connections between all the relevant cells of each T4 were traced, i.e., connections between L1 and Mi1/Tm3 and the downstream connections from Mi1/Tm3 to T4. In this way, the T4 inputs can be mapped as if onto a columnar array of L1s, and hence into the visual field. These tracings were performed in the expanded reconstruction volume of 19 medulla columns (one central and 18 surrounding columns).

The T4 receptive fields of Mi1- and Tm3-mediated components were calculated as follows: the number of synaptic contacts from each L1 to an intermediate Mi1 is multiplied by the number of contacts from the Mi1 to T4 (Fig. 3b). Similarly, the number of contacts from each L1 to intermediate Tm3s is multiplied by the number of contacts from the Tm3s to T4, and then summed over all the Tm3 neurons that receive input from the same L1. This multiplication is equivalent to counting the number of independent synaptic routes from each L1 to each T4, in which each route must use a different pair of the synaptic contacts between the L1 and the intermediate target neurons, and the intermediate targets and the T4. These calculations revealed that, although the anatomical dendritic map of Mi1 and Tm3 shows substantial overlaps, T4 receptive fields of Mi1- and Tm3-mediated components are significantly displaced (Fig. 3c).

T4 receptive fields offset correlates with the direction preference

Is the direction of displacement between the Mi1 and Tm3 receptive field components for a T4 consistent with the direction preference of the T4? First, to determine the direction preference of T4 cells, 19 T4s were selected for their locations close to the central column, and then their axons were traced. Of these, 16 were successfully traced down to the lobula plate. These axon tracings determined the direction preferences of those T4s by their terminal arbor depth in the lobula plate (Fig. 3b). Then, in the absence of evidence for synaptic polarity onto T4s, the vector of receptive field offset is arbitrarily defined as the direction from the center of mass of the Tm3 component to that of the Mi1 component. This assumption adequately leads to the spatial displacements consistent with the direction preference of the T4s (Fig. 3b and c).

Assuming that the Mi1 and Tm3 inputs to T4 are the same excitatory synapses, as in the Hassenstein–Reichardt EMD model, the Tm3 arm of the motion detector should introduce a longer delay than the Mi1 arm. Conversely, if the inputs were combined with opposing signs, as in the alternative model, the Barlow–Levick EMD model, which was suggested from the experimental findings of direction-selective ganglion cells in the rabbit retina [60], then the prediction would be reversed. A recent study of whole-cell patch recording has shown significant temporal offset between Mi1 and Tm3, with Mi1 exhibiting a delayed response compared with Tm3 [61]. Considering these response properties of Mi1 and Tm3, T4's directional selectivity is likely accomplished by combining Mi1 and Tm3 inputs with opposite signs, as in the Barlow–Levick model.

Morphological feature differentiating T4 subtypes

There is an additional observation on T4's anatomy. Close examination of the T4 dendritic processes in the proximal medulla (stratum M10) revealed that their branching arbors are oriented primarily in one direction [41]. Furthermore, the branch orientation of each T4 clusters around one of four directions, when measured from the branch tip to the axon main trunk. This observation reconfirmed the classification of each T4 into direction preference subtypes which was determined by its terminal arbor depth in the lobula plate. This characterization was then used to infer a direction preference for the remaining three T4 cells, for which tracing into the lobula plate failed. At the place of signal convergence on T4 dendrites, there might be an additional or alternative implementation of relative delay: since T4 cells express both ionotropic and metabotropic cholinoceptors as shown by single-cell transcript profiling, these could mediate a fast and slow signal, respectively [34].

Comprehensive and detailed map of synaptic connections

Here, in the connectomics study in *Drosophila*, a small chunk of neuropil was initially targeted and automatically segmented for a dense, volumetric reconstruction. Subsequently, the reconstruction volume was expanded to examine additional neurons and synapses of particular interest, which were selectively and sparsely traced. The advantage of the dense reconstruction is that it enables us a comprehensive analysis of neural circuits and to argue both the presence and absence of strong connections between any two cell types [41]. On the other hand, the sparse reconstruction permits us to determine the inputs to a particular neuron or a brain region more quickly by skeletonizing neurons [62–65]. The medulla reconstruction demonstrated that these two approaches are not mutually exclusive.

Conclusions and outlook

The connectome reconstruction in the *Drosophila* optic medulla removed a longstanding block to understanding the exact mechanism of motion detection, by identifying the underlying concrete neural elements and circuits. The connectomic approach proved the importance of mapping the entire synaptic connections in the region of interest, showing that it can tell which types of cells are involved and which types are not involved in a particular neural computation. Further, more generally, the study illustrates that connectomes can, by identifying the underlying circuits, provide key insight into neuronal computation.

When driving a car, a global positioning system with full map information is appreciated when trying to get to the destination via the shortest route. Likewise, it is essential to have a full connectome map of the brain, to analyze functions or identify the cause of diseases brought about by abnormal neural circuits. This is precisely what connectomics aims at. One obstacle is scaling up, however. How can we make the jump from the small-scale circuits analyzed thus far to the whole brain? This will require a lot of both work and patience, but the effort practiced in the *Drosophila* connectomics should keep evolving as the reconstruction strategy, analysis tools and software, and imaging and automation technologies advance. These developments and improvements will also be applicable to larger-scale connectomics, including mammalian brains.

One area that is currently being greatly improved is EM imaging. Imaging with better resolution than the minimum required should provide enormous benefit for automation processes. FIB-SEM offers the best z-resolution and is the only technique that allows isotropic image datasets. In preliminary results, the automated segmentation on FIB-SEM data exhibits near-human performance. Moreover, although the limited field of view of FIB-SEM has been a concern, a

new strategy of lossless thick sectioning of embedded brain tissue by hot-knife technology is being established, where a large sample block can be losslessly cut into optimally sized pieces for parallel FIB-SEM imaging (K. J. Hayworth et al., submitted for publication). FIB-SEM thus could provide an avenue for scalable high-resolution imaging efforts. A complete brain connectome of *Drosophila* is now being contemplated, generating a whole brain dataset.

Acknowledgements

I am indebted to all the members in the Janelia FlyEM project team for their contributions and support and also grateful to Lou and Lucynda Scheffer for reading the manuscript and for helpful comments. The project was supported by the Howard Hughes Medical Institute.

References

1. Keene A C, Waddell S (2007) *Drosophila* olfactory memory: single genes to complex neural circuits. *Nat. Rev. Neurosci.* 8: 341–354.
2. Dickson B J (2008) Wired for sex: the neurobiology of *Drosophila* mating decisions. *Science* 322: 904–909.
3. Olsen S R, Wilson R I (2008) Cracking neural circuits in a tiny brain: new approaches for understanding the neural circuitry of *Drosophila*. *Trends Neurosci.* 31: 512–520.
4. Venken K J T, Simpson J H, Bellen H J (2011) Genetic manipulation of genes and cells in the nervous system of the fruit fly. *Neuron* 72: 202–230.
5. Silies M, Gohl D M, Clandinin T R (2014) Motion-detecting circuits in flies: Coming into view. *Annu. Rev. Neurosci.* 37: 307–327.
6. Borst A (2014) Fly visual course control: behaviour, algorithms and circuits. *Nat. Rev. Neurosci.* 15: 590–599.
7. Hassenstein B, Reichardt W (1956) Systemtheoretische Analyse der Zeit-, Reihenfolgen- und Vorzeichenauswertung bei der Bewegungsperzeption des Rüsselkäfers *Chlorophanus*. *Z. Naturforsch. B* 11: 513–524.
8. Reichardt W (1961) Autocorrelation, a principle for the evaluation of sensory information by the central nervous system. In: Rosenblith W A (ed.), *Sensory Communication*, pp. 303–317, (MIT Press, New York).
9. Borst A, Egelhaaf M (1989) Principles of visual motion detection. *Trends Neurosci.* 12: 297–306.
10. Poggio T, Reichardt W (1976) Visual control of orientation behaviour in the fly: part II. Towards the underlying neural interactions. *Q. Rev. Biophys.* 9: 377–438.
11. Adelson E H, Bergen J R (1985) Spatiotemporal energy models for the perception of motion. *J. Opt. Soc. Am. A* 2: 284–299.
12. Hildreth E C, Koch C (1987) The analysis of visual motion: from computational theory to neuronal mechanisms. *Annu. Rev. Neurosci.* 10: 477–533.
13. Potters M, Bialek W (1994) Statistical mechanics and visual signal processing. *J. Phys. I (France)* 4: 1755–1775.
14. Buchner E (1976) Elementary movement detectors in an insect visual system. *Biol. Cybern.* 24: 85–101.
15. Buchner E (1984) Behavioural analysis of spatial vision in insects. In: Ali M A (ed.), *Photoreception and Vision in Invertebrates*, pp. 561–621, (Plenum Press, New York).
16. Borst A, Egelhaaf M (1987) Temporal modulation of luminance adapts time constant of fly movement detectors. *Biol. Cybern.* 56: 209–215.
17. Egelhaaf M, Reichardt W (1987) Dynamic-response properties of movement detectors: theoretical-analysis and electrophysiological investigation in the visual-system of the fly. *Biol. Cybern.* 56: 69–87.
18. Egelhaaf M, Borst A (1989) Transient and steady-state response properties of movement detectors. *J. Opt. Soc. Am. A* 6: 116–127.
19. Egelhaaf M, Borst A, Reichardt W (1989) Computational structure of a biological motion-detection system as revealed by local detector analysis in the fly's nervous system. *J. Opt. Soc. Am. A* 6: 1070–1087.
20. Schuling F H, Mastebroek H A K, Bult R, Lenting B P M (1989) Properties of elementary movement detectors in the fly *Calliphora erythrocephala*. *J. Comp. Physiol. A* 165: 179–192.
21. Zanker J M, Srinivasan M V, Egelhaaf M (1999) Speed tuning in elementary motion detectors of the correlation type. *Biol. Cybern.* 80: 109–116.
22. Borst A, Flanagin V L, Sompolinsky H (2005) Adaptation without parameter change: dynamic gain control in motion detection. *Proc. Natl. Acad. Sci. USA* 102: 6172–6176.
23. Clark D A, Bursztyn L, Horowitz M A, Schnitzer M J, Clandinin T R (2011) Defining the computational structure of the motion detector in *Drosophila*. *Neuron* 70: 1165–1177.
24. Eichner H, Joesch M, Schnell B, Reiff D F, Borst A (2011) Internal structure of the fly elementary motion detector. *Neuron* 70: 1155–1164.
25. Laughlin S B, Hardie R C (1978) Common strategies for light adaptation in the peripheral visual systems of fly and dragonfly. *J. Comp. Physiol. A* 128: 319–340.
26. Laughlin S B (1994) Matching coding, circuits, cells, and molecules to signals: general principles of retinal design in the fly's eye. *Prog. Retin. Eye Res.* 13: 165–196.
27. Zheng L, de Polavieja G G, Wolfram V, Asyali M H, Hardie R C, Juusola M (2006) Feedback network controls photoreceptor output at the layer of first visual synapses in *Drosophila*. *J. Gen. Physiol.* 127: 495–510.
28. Zheng L, Nikolaev A, Wardill T J, O'Kane C J, de Polavieja G G, Juusola M (2009) Network adaptation improves temporal representation of naturalistic stimuli in *Drosophila* eye: I Dynamics. *PLoS ONE* 4: e4307.
29. Joesch M, Plett J, Borst A, Reiff D F (2008) Response properties of motion-sensitive visual interneurons in the lobula plate of *Drosophila* melanogaster. *Curr. Biol.* 18: 368–374.
30. Krapp H G, Hengstenberg R (1996) Estimation of self-motion by optic flow processing in single visual interneurons. *Nature* 384: 463466.
31. Meinertzhagen I A, Sorra K E (2001) Synaptic organisation in the fly's optic lamina: few cells, many synapses and divergent microcircuits. *Prog. Brain Res.* 131: 53–69.
32. Takemura S Y, Lu Z, Meinertzhagen I A (2008) Synaptic circuits of the *Drosophila* optic lobe: the input terminals to the medulla. *J. Comp. Neurol.* 509: 493–513.
33. Rivera-Alba M, Vitaladevuni S, Mishchenko Y, Lu Z, Takemura S Y, Scheffer L K, Meinertzhagen I A, Chklovskii D B,

de Polavieja G G (2011) Wiring economy and volume exclusion determine neuronal placement in the *Drosophila* brain. *Curr. Biol.* 21: 2000–2005.
34. Shinomiya K, Karuppudurai T, Lin T Y, Lu Z, Lee C H, Meinertzhagen I A (2014) Candidate neural substrates for off-edge motion detection in *Drosophila*. *Curr. Biol.* 24: 1062–1070.
35. Rister J, Pauls D, Schnell B, Ting C Y, Lee C H, Sinakevitch I, Morante J, Strausfeld N J, Ito K, Heisenberg M (2007) Dissection of the peripheral motion channel in the visual system of *Drosophila* melanogaster. *Neuron* 56: 155–170.
36. Joesch M, Schnell B, Raghu S V, Reiff D F, Borst A (2010) ON and OFF pathways in *Drosophila* motion vision. *Nature* 468: 300–304.
37. Meinertzhagen I A, O'Neil S D (1991) Synaptic organization of columnar elements in the lamina of the wild type in *Drosophila* melanogaster. *J. Comp. Neurol.* 305: 232–263.
38. Douglass J K, Strausfeld N J (2003) Anatomical organization of retinotopic motion-sensitive pathways in the optic lobes of flies. *Microsc. Res. Tech.* 62: 132–150.
39. Borst A, Haag J, Reiff D F (2010) Fly motion vision. *Annu. Rev. Neurosci.* 33: 49–70.
40. Fischbach K-F, Dittrich A P M (1989) The optic lobe of *Drosophila melanogaster*. I. A Golgi analysis of wild-type structure. *Cell Tissue Res.* 258: 441–475.
41. Takemura S Y, Bharioke A, Lu Z, Nern A, Vitaladevuni S, Rivlin P K, Katz W T, Olbris D J, Plaza S M, Winston P, et al. (2013) A visual motion detection circuit suggested by *Drosophila* connectomics. *Nature* 500: 175–181.
42. White J G, Southgate E, Thomson J N, Brenner S (1986) The structure of the nervous system of the nematode *Caenorhabditis elegans*. *Phil. Trans. R. Soc. Lond. B* 314: 1–340.
43. Denk W, Heinz H (2004) Serial block-face scanning electron microscopy to reconstruct three-dimensional tissue nanostructure. *PLoS Biol.* 2: e329.
44. Knott G, Marchman H, Wall D, Lich B (2008) Serial section scanning electron microscopy of adult brain tissue using focused ion beam milling. *J. Neurosci.* 28: 2959–2964.
45. Chklovskii D B, Vitaladevuni S, Scheffer L K (2010) Semi-automated reconstruction of neural circuits using electron microscopy. *Curr. Opin. Neurobiol.* 20: 667–675.
46. Sosinsky G E, Crum J, Jones Y Z, Lanman J, Smarr B, Terada M, Martone M E, Deerinck T J, Johnson J E, Ellisman M H (2008) The combination of chemical fixation procedures with high pressure freezing and freeze substitution preserves highly labile tissue ultrastructure for electron tomography applications. *J. Struct. Biol.* 161: 359–371.
47. Scheffer L K, Karsh B, Vitaladevuni S (2013) Automated alignment of imperfect EM images for neural reconstruction. Preprint at http://arXive.org/abs/1304.6034.
48. Canny J (1986) A computational approach to edge detection. *IEEE Trans. Pattern Anal. Mach. Intell.* 8: 679–698.
49. Vincent L, Soille P (1991) Watersheds in digital spaces: an efficient algorithm based on immersion simulations. *IEEE Trans. Pattern Anal. Mach. Intell.* 13: 583–598.
50. Soille P (2003) *Morphological Image Analysis: Principles and Applications*, 2nd ed., (Springer-Verlag, New York).
51. Martin D R, Fowlkes C C, Malik J (2004) Learning to detect natural image boundaries using local brightness, color, and texture cues. *IEEE Trans. Pattern Anal. Mach. Intell.* 26: 530–549.
52. Dollar P, Tu Z, Belongie S (2006) Supervised learning of edges and object boundaries. *IEEE Comp. Soc. Conf. Comp. Vis. Pattern Rec.* 2: 1964–1971.
53. Mishchenko Y (2009) Automation of 3D reconstruction of neural tissue from large volume of conventional serial section transmission electron micrographs. *J. Neurosci. Methods* 176: 276–289.
54. Van Eck N J, Waltman L (2007) VOS: a new method for visualizing similarities between objects. *Adv. Data Anal.* 299–306.
55. Buchner E, Buchner S, Bülthoff I (1984) Deoxyglucose mapping of nervous activity induced in *Drosophila* brain by visual movement. *J. Comp. Physiol. A* 155: 471–483.
56. Strausfeld N J, Lee J K (1991) Neuronal basis for parallel visual processing in the fly. *Vis. Neurosci.* 7: 13–33.
57. Bausenwein B, Fischbach K F (1992) Activity labelling patterns in the medulla of *Drosophila* melanogaster caused by motion stimuli. *Cell Tissue Res.* 270: 25–35.
58. Schnell B, Raghu S V, Nern A, Borst A (2012) Columnar cells necessary for motion responses of wide-field visual interneurons in *Drosophila*. *J. Comp. Physiol. A* 198: 389–395.
59. Maisak M S, Haag J, Ammer G, Serbe E, Meier M, Leonhardt A, Schilling T, Bahl A, Rubin G M, Nern A, et al. (2013) A directional tuning map of *Drosophila* elementary motion detectors. *Nature* 500: 212–216.
60. Barlow H B, Levick W R (1965) The mechanism of directionally selective units in rabbit's retina. *J. Physiol.* 178: 477–504.
61. Behnia R, Clark D A, Carter A G, Clandinin T R, Desplan C (2014) Processing properties of ON and OFF pathways for *Drosophila* motion detection. *Nature* 512: 427–430.
62. Saalfeld S, Cardona A, Hartenstein V, Tomančák P (2009) CATMAID: collaborative annotation toolkit for massive amounts of image data. *Bioinformatics* 25: 1984–1986.
63. Jeong W K, Beyer J, Hadwiger M, Blue R, Law C, Vazquez-Reina A, Reid R C, Lichtman J, Pfister H. (2010) Ssecrett and NeuroTrace: interactive visualization and analysis tools for large-scale neuroscience data sets. *IEEE Comput. Graph Appl.* 30: 58–70.
64. Helmstaedter M, Briggman K L, Denk W (2011) High-accuracy neurite reconstruction for high-throughput neuroanatomy. *Nat. Neurosci.* 14: 1081–1088.
65. Xu M, Jarrell T A, Wang Y, Cook S J, Hall D H, Emmons S W (2013) Computer assisted assembly of connectomes from electron micrographs: application to *Caenorhabditis elegans*. *PLoS ONE* 8: e54050.